

# TRACING THE [FeII]/[NeII] RATIO AND ITS RELATIONSHIP WITH OTHER ISM INDICATORS WITHIN STAR FORMING DWARF GALAXIES: A *SPITZER* IRS ARCHIVAL STUDY.

B. O'HALLORAN<sup>1</sup>, S. C. MADDEN<sup>2</sup>, N. P. ABEL<sup>3</sup>

*Draft version March 20, 2008*

## ABSTRACT

Archival *Spitzer* observations of 41 starburst galaxies that span a wide range in metallicity reveal for the first time a correlation between the [FeII]/[NeII] 26.0/12.8  $\mu\text{m}$  ratio and the electron gas density as traced by the 18.7/33.4  $\mu\text{m}$  [SIII] ratio, with the [FeII]/[NeII] ratio decreasing with increasing gas density. The correlations of the [FeII]/[NeII] ratio, the PAH peak to continuum strength & metallicity found in an earlier paper were confirmed for a larger sample. We also find a strong correlation between the gas density and the PAH peak to continuum strength. Using shock and photoionization models, we see the driver of the observed [FeII]/[NeII] ratios is metallicity. The majority of [FeII] emission in low metallicity galaxies may be shock-derived, whilst at high metallicity, the [FeII] emission may be instead dominated by contributions from H II and in particular from dense PDR regions. However, the observed [FeII]/[NeII] ratios may instead be following a metallicity-abundance relationship, with iron being less depleted onto grains in low metallicity galaxies - a result that would have profound implications for the use of iron emission lines as unambiguous tracers of shocks.

*Subject headings:* galaxies: starburst - galaxies: stellar content - ISM: lines and bands - infrared: galaxies

## 1. INTRODUCTION

The presence of massive stars within starbursts undoubtedly plays a huge role in determining the physical conditions within the local interstellar medium (ISM). High-mass ( $M_{\text{init}} \geq 8M_{\odot}$ ) stars formed within typical starbursts drastically affect the dynamics of the surrounding ISM, through not only the release of ionizing photons which destroy molecular material, but also via supernovae (SNe) which provide thermal and kinetic energy input into the ISM. The effects of photoionization by high-mass stars on the observed dearth of PAHs have recently been investigated (Madden et al. 2006; Wu et al. 2006), while in O'Halloran, Satyapal & Dudik (2006) (hereafter Paper I), we examined a sample of 18 galaxies of varying metallicity (from 1/50th to super solar) with high star formation rates in order to determine whether supernova-driven shocks do indeed play a role in the PAH deficit in low metallicity environments. If we consider the ratio of the 26  $\mu\text{m}$  [FeII] line and the 12.8  $\mu\text{m}$  [NeII] line as a tracer of the strength of supernova shocks, we found a strong anti-correlation suggesting that strong supernova-driven shocks are indeed present within low metallicity galaxies. Furthermore, the PAH deficit within these objects may indeed be linked to the presence and strength of these shocks. However, it has not as yet been conclusively proved that shocks are the dominant process behind the PAH deficit. As already noted, photoionization and perhaps delayed injection of dust into the ISM (Galliano 2008) each make their own contributions to the PAH deficit, but as yet, it remains unclear as to which of these three processes is the most

dominant. Additionally, is the relationship between the [FeII]/[NeII] ratio and the PAH emission, as indicated in Paper I, really probing a causal effect? It could very well be that this relationship may be coincidental, or that physical or selection effects may be the primary drivers for the observed relationship. It would therefore be advisable to further explore the nature of the ISM within such star-forming environments using additional mid-IR probes in order to expand upon our understanding of the [FeII]/[NeII] ratio, and by extension, its relationship with key ISM indicators such as PAH strength and metallicity.

## 2. OBSERVATIONS AND DATA ANALYSIS

To accomplish this, we have expanded our sample from the 18 objects presented in Paper I by including archival IRS observations of 23 additional objects, bringing the sample total to 41. The full list of targets is given in Table 1, and listed by increasing metallicity. These galaxies range in metallicity from extremely low (such as I Zw 18, with  $Z/Z_{\odot} = 1/50$ ) to super-solar metallicity ( $\geq 1 Z_{\odot}$ ) galaxies such as NGC 7714. To differentiate between low and high-metallicity galaxies, we use a metallicity ( $12 + \log [\text{O}/\text{H}]$ ) cut-off value of 8.85 - just less than solar, as per Paper I. The galaxies range widely in morphology from blue compact dwarfs such as I Zw 18 to spirals such as NGC 7714 and IC 342. None of the galaxies in our sample are known to harbour AGNs. This is important, as PAH destruction can occur close to an AGN due to the hard ionization environment (e.g. Sturm et al. 2000). In addition [FeII] emission can be elevated in galaxies harbouring AGN. One possible exception is NGC 7714, which is optically classified as a LINER (Thomas et al. 2002). However, the lack of [NeV] emission at 14 and 24  $\mu\text{m}$  and the absence of any evidence for an obscured AGN by recent Chandra imaging (Brandl et al. 2004; Smith et al. 2005) strongly suggests that NGC 7714 is a pure starburst and it is therefore included in our sample.

Electronic address: boh@physics.gmu.edu

<sup>1</sup> Dept. of Physics & Astronomy, George Mason University, Fairfax, VA 22030, USA

<sup>2</sup> Service d'Astrophysique, CEA, Saclay, Orme des Merisiers 91191, Gif-sur-Yvette, France

<sup>3</sup> Department of Physics, University of Cincinnati, Cincinnati, OH 45221, USA

We extracted low and high resolution archival spectral data from the Short-Low (SL) (5.2 - 14.5  $\mu\text{m}$ ), Short-High (SH) (9.9 - 19.6  $\mu\text{m}$ ) and Long-High (LH) (18.7 - 37.2  $\mu\text{m}$ ) modules of the *Spitzer* Infrared Spectrograph (IRS). The datasets were derived from a number of *Spitzer* Legacy, GO and GTO programs released to the *Spitzer* Data Archive, and consisted of either spectral mapping or staring observations. We obtained fluxes for the nuclear positions only from the mapping observations. All the staring observations were centered on the galaxy's nucleus. The data were preprocessed by the *Spitzer* Science Center (SSC) data reduction pipeline version 15.3<sup>4</sup> before being downloaded. Further processing was done within the IRS BCD-level data reduction package *SPICE*, v 2.0.1<sup>5</sup>. Both the low and high resolution spectra were extracted by *SPICE* using the full-aperture extraction method. As the [SIII] emission is extended beyond the extent of the high resolution slits in particular, we applied the ALCF and SLCF extended source corrections to the spectra as part of the *SPICE* extraction<sup>6</sup>. The slit for the SH and LH modules is too small for background subtraction to take place and separate SH or LH background observations do not exist for any of the galaxies in this sample. For the SL module, background subtraction was done using either a designated background file when available or by subtracting the data from one nod position from the other along the slit. In some cases, the slit was enveloped in the host galaxy and background subtraction could not take place. For both high and low resolution spectra, the ends of each order where the noise increases significantly were manually clipped, as were hot pixels.

For the high resolution observations, we required matched extractions in terms of angular extent from both the SH & LH slits, in order to accurately derive densities based upon the 18 and 33  $\mu\text{m}$  [SIII] lines. The ionization potential of [SIII] is  $\sim 35$  eV, with the [SIII] emission arising from gas ionized by young stars for our sample. With a relatively low ionization potential, [SIII] emission may be quite easily extended in spatial extent beyond the nuclear single-slit pointings for SH and LH. Indeed, comparisons of ISO and IRS data (Dudik 2007) show [SIII] emission within star-forming AGN that extends beyond the size of both the SH and LH slits. Given that [SIII] emission is extended and we would expect to see a higher flux in the larger LH slit, any derived [SIII] line ratio will be artificially depressed. To avoid such aperture effects between the SH and LH slits, we scaled the LH flux by multiplying it by the ratio of the SH/LH slit angular sizes.

As a number of the sample starbursts at high metallicity are known to be dusty systems with large obscuration, the extracted line fluxes were then corrected for extinction for the sample as a whole. The fluxes and statistical errors, plus the derived line ratios, are presented in Tables 1 and 2 respectively, obtained using the IDL-based analysis package *SMART*, v.6.2.6 (Higdon et al. 2004). In all cases detections were defined when the line flux was at least  $3\sigma$ . For the SL, SH and LH modules the spectral

resolution was  $\lambda/\delta\lambda$  60-127 and  $\sim 600$  respectively, with FWHM in the order of  $1.9 \times 10^{-1} \mu\text{m}$  for the PAH feature in the low-res spectrum, and  $2-4 \times 10^{-2} \mu\text{m}$  for the fine structure lines in the high resolution spectra. For the absolute photometric flux uncertainty we conservatively adopt 15%, based on the assessed values given by the *Spitzer* Science Center (SSC) over the lifetime of the mission. This error is calculated from multiple observations of various standard stars throughout the *Spitzer* mission by the SSC. The dominant component of the total error arises from the uncertainty at mid-IR wavelengths in the stellar models used in calibration and is systematic rather than Gaussian in nature. The 6.2  $\mu\text{m}$  PAH strength was determined according to the prescription adopted in a number of previous studies (Rigoupolou et al. 1999; Förster Schreiber et al. 2004). While the 7.7 and 8.6  $\mu\text{m}$  PAH lines are stronger, the 8.6  $\mu\text{m}$  line can suffer extinction effects due to a potential silicate absorption feature at 9  $\mu\text{m}$ , and both of these pose difficulties in determining the continuum level. For this work, the continuum was determined at the center of the 6.2  $\mu\text{m}$  feature, using a first order linear fit to the 5.5 and 11.5  $\mu\text{m}$  bandpass. The PAH strength was then calculated as the ratio of the 6.2  $\mu\text{m}$  feature peak intensity to the underlying continuum. We assume a Gaussian fit while fitting the PAH and fine structure lines with *SMART*.

### 3. RESULTS

In Fig 1, we plot [FeII]/[NeII] vs the 6.2  $\mu\text{m}$  PAH peak to continuum ratio to check if the relationship between the [FeII]/[NeII] ratio and the PAH peak to continuum strength first noted in Paper I, using the 6.2  $\mu\text{m}$  PAH feature instead of the 7.7  $\mu\text{m}$ , as one can perform continuum fitting with a higher degree of confidence with the 6.2  $\mu\text{m}$  feature, still holds for the expanded sample, as noted above. Employing a Spearman rank correlation analysis (Kendall & Stuart 1976) to assess the statistical significance of this trend yields a correlation coefficient of  $r_s$  of -0.705 and  $P_s$  of  $2.69 \times 10^{-6}$ , confirming the significant anti-correlation between PAH strength and the [FeII]/[NeII] ratio as seen in Paper I. The Spearman rank correlation technique has the advantage of being non-parametric, robust to outliers and does not presuppose a linear relation. We plot the [FeII]/[NeII] ratio versus the metallicity in Fig.2, and we again see a strong anti-correlation ( $r_s$  of -0.777 and  $P_s$  of  $9.36 \times 10^{-7}$ ) between [FeII]/[NeII] and metallicity as seen in paper I.

Based upon what we have already seen from Paper I and from Figs. 1 and 2, if the [FeII]/[NeII] ratio is truly indicative of the strength of supernova-driven shocks within the extent of the high resolution slits, one would expect the passage of such shocks to affect conditions within the local ISM in quite a substantive manner. Shocks, in addition to removing dust and PAH from the ISM (Reach & Rho 2000; Reach et al. 2006), should also be adept in removing gas - one would therefore expect the propagation of intense SNe-driven shocks into the ISM of star forming regions to greatly impact on the density of the gas. In order to determine how the gas density within these nuclear star forming regions corresponds with the strength of the supernova-driven shocks, we require a reliable mid-IR tracer to probe the gas density. The [SIII] 18.7/33.4  $\mu\text{m}$  line ratio provides such a reliable mid-IR tracer of the gas density, as it is ideal

<sup>4</sup> *Spitzer* Observers Manual, URL: <http://ssc.spitzer.caltech.edu/documents/som/>

<sup>5</sup> URL: <http://ssc.spitzer.caltech.edu/postbcd/spice.html>

<sup>6</sup> URL: <http://ssc.spitzer.caltech.edu/postbcd/doc/spice.pdf>

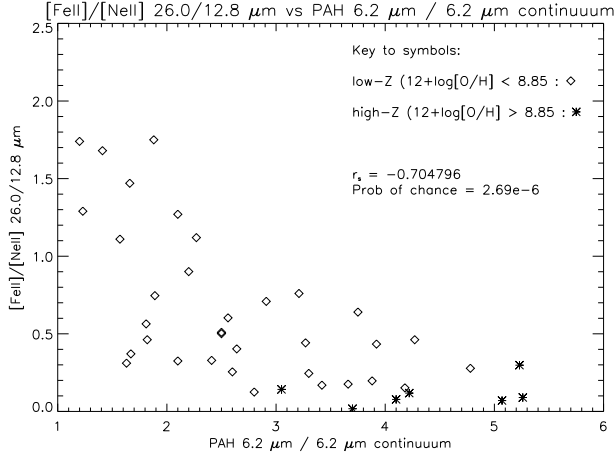


FIG. 1.— Plot of the [FeII]/[NeII] ratio versus the PAH 6.2 micron peak to continuum ratio for the extended sample. The observed trend confirms the relationships between the [FeII]/[NeII] ratio and the PAH strength seen in Paper I.

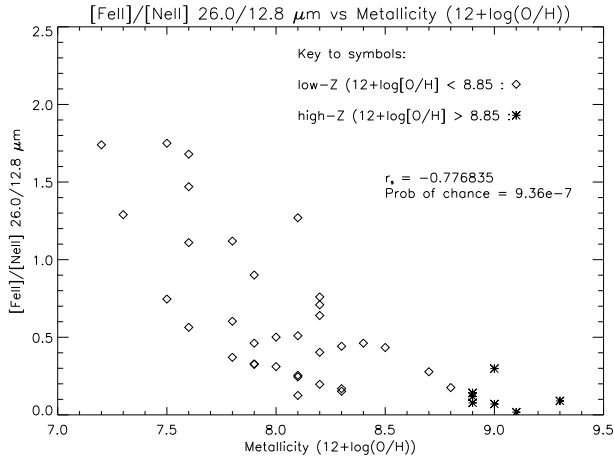


FIG. 2.— Plot of the [FeII]/[NeII] ratio versus the metallicity for the extended sample. The observed trend confirms the strong relationship between the [FeII]/[NeII] ratio and metallicity seen in Paper I.

for probing gas (with high critical densities) in the regions surrounding starbursts, especially as the [SIII] lines are starburst dominated (Verma et al. 2004). This ratio is sensitive to changes in the density for the  $50 \leq n_e \leq 10^4 \text{ cm}^{-3}$ , but is insensitive to changes in temperature (Rigopoulou et al. 1996). In Fig. 3, we plot the logarithm of the ratio of the [SIII] fluxes versus the [FeII]/[NeII] flux ratio. There is a strikingly strong trend between the two line ratios, with high [FeII]/[NeII] values corresponding to lower [SIII] ratios. Using the Spearman rank correlation analysis, we get ( $r_s$ ) of -0.891 between the [SIII] ratio and the [FeII]/[NeII] with a probability of chance correlation ( $P_s$ ) of  $7.43 \times 10^{-8}$ , indicating a significant anti-correlation. Interestingly, we see a general decrease in the metallicity of the object with lower [SIII] ratios, corresponding to higher [FeII]/[NeII].

We again plot the logarithm of the ratio of the [SIII] fluxes in Fig. 4, but this time against the 6.2 micron PAH peak/continuum ratio. As with Fig. 3, we see a strong trend, but this time with the PAH strength in-

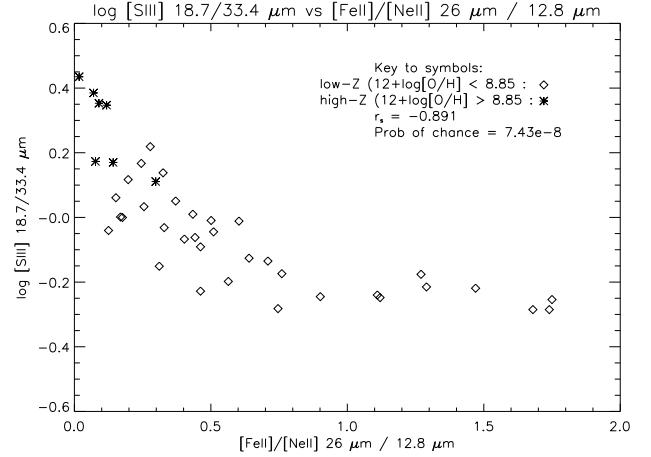


FIG. 3.— Plot of the 18.7/33.4  $\mu\text{m}$  [SIII] ratio as a function of the [FeII]/[NeII] ratio for the extended sample. The [SIII] ratio correlates strongly with the [FeII]/[NeII] ratio, with high values of the [FeII]/[NeII] ratio corresponding to low [SIII] ratios and metallicity.

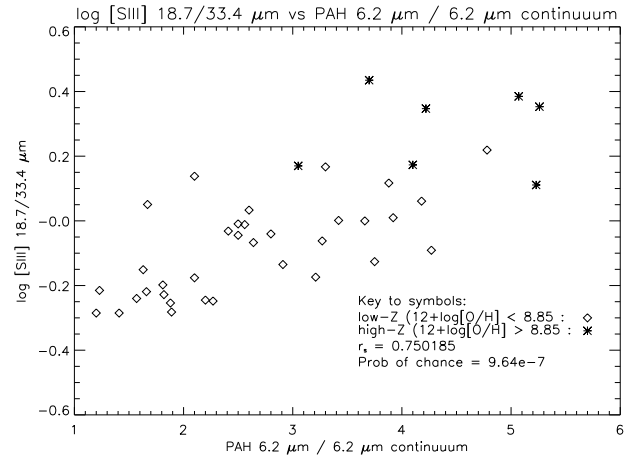


FIG. 4.— Plot of the 18.7/33.4  $\mu\text{m}$  [SIII] ratio as a function of the 6.2  $\mu\text{m}$  PAH peak to continuum strength for the extended sample. The [SIII] ratio correlates quite well with the PAH strength, indicating that the gas density scales with the increased strength of PAH emission.

creasing with log [SIII] - the PAH strength is increasing with higher gas density. Again running a Spearman rank correlation analysis, we get  $r_s$  of 0.750 and  $P_s$  of  $9.64 \times 10^{-7}$ , confirming a significant correlation between log [SIII] and PAH strength. We again see that a general trend exists with PAH strength increasing with metallicity and increasing values of log [SIII].

#### 4. DISCUSSION

##### 4.1. Can we explain the observed relationships?

##### 4.1.1. Are there other factors which may be influencing the observed relationships?

As we have seen from Figs. 1-4, a series of relationships would seem to exist between the [FeII]/[NeII] ratio, the metallicity, the PAH strength and the [SIII] ratio, with low values of the [SIII] ratio corresponding with high [FeII]/[NeII] ratios and weak/no PAH emission. However, before we press ahead with more detailed investigations of the nature of these relationships, it is prudent

to first check whether other factors, such as extinction and aperture effects might be responsible.

#### 4.1.2. Extinction

As we have noted previously in Section 2, we corrected the IRS fluxes for extinction, with  $A_V$  ranging from  $\sim 2$  to 30 mag. To determine the correction, we used the ratios of  $H\beta/H\alpha$  and  $Br\beta/Br\alpha$  where available from the literature. Emissivity coefficients from Storey & Hummer (1995) for case B recombination with an electron temperature of  $10^4$  K and density of  $100 \text{ cm}^{-3}$  were used to calculate the intrinsic line ratios for the H recombination lines. We note that while the density used in these calculations is lower than that seen in some of our sample, we noted little change in the intrinsic line ratios for denser environments. We adopted a Draine (1989) extinction law above  $8.5 \mu\text{m}$ , and the Lutz, Veilleux & Genzel (1999) galactic extinction law below this point. As the observed relationships remain post correction, we conclude that extinction can be ruled out as a driver for the observed correlations. For the optical [SII] lines used lines used as comparisons to the *MAPPINGS* output, we obtained and used from the literature extinction corrected fluxes where available.

#### 4.1.3. Aperture effects

As noted earlier, the ionization potential of [SIII] is  $\sim 35$  eV, with the [SIII] emission arising from gas ionized by young stars. With a relatively low ionization potential, [SIII] emission may be quite easily extended in spatial extent beyond the nuclear single-slit pointings for SH and LH. To compensate, we applied the SLCF and ALCF extended source corrections to the spectra. Additionally, as we are looking to derive a physical quantity, namely the gas density, over a similarly sized physical area given the extent of the [SIII] emission, it is therefore crucial that we use [SIII] fluxes derived from slits of equal angular size. To do this, we obtained a fraction of the LH full slit flux by multiplying it by the SH/LH angular size ratio, as noted in Section 2. The final, corrected fluxes are given in Table 1.

### 4.2. Modeling the observed relationships

Since we can rule out extinction and aperture effects as drivers for the observed correlations, we can be confident that the correlations seen in Figs. 1-4 are indeed true physical relationships between the strength of the [FeII]/[NeII] ratio and a number of ISM ingredients, with the primary culprit for the observed relationships being the passage of SNe-driven shocks. However, while we have focussed up to now with a supernova-derived shock origin for the behaviour of the [FeII]/[NeII] ratio, it may not be the only explanation. For example, Izotov et al. (2006) note sign of strong depletion of iron onto dust grains, and gradual destruction of those grains on a time scale of a few Myr, based on a survey of metal-poor galaxies from the 3rd release of the SDSS. Such a process could undoubtedly drastically affect the nature of Fe emission, and by extension the behaviour of the [FeII]/[NeII] ratio, within our sample - we may instead be probing an abundance-driven relationship and the other observed relationships presented here would be purely coincidental to the [FeII]/[NeII] ratio. In order to explore if this

indeed is the true cause or if shocks alone can explain the observed relationships, we used shock and standard H II - PDR models in an effort to model the observed [FeII]/[NeII] relationship for a wide variety of environments. We used both the *MAPPINGS III* photoionization/shock code (Sutherland & Dopita 1993) and the Cloudy photoionization code (Ferland et al. 1998) in order to determine the relative proportions to the [FeII] emission from shocks and H II/PDRs, and by extension, the driving process behind the behaviour of the observed [FeII]/[NeII] line ratio. In addition to the mid-IR output, we also wished to explore if a similar relationship is present at optical wavelengths. To this end, we use the ratio of extinction corrected [SII] fluxes at 6716 and 6731 Å taken from the literature and compared the observed ratios with the *MAPPINGS* output.

#### 4.2.1. *MAPPINGS* models

In an effort to quantify the true nature of the [FeII]/[NeII] ratio, we initially constructed a number of *MAPPINGS* models where density, metallicity and luminosity were allowed to vary. The theoretical H II region models were generated by the *MAPPINGS III* code, which uses as input the EUV fields predicted by the stellar population synthesis models *STARBURST99* (Leitherer et al. 1999). The photoionization modeling and shock models carried out with *MAPPINGS III* for this analysis are described in Dopita & Sutherland (1996) and Kewley et al. (2001), and are described briefly here. To model the H II region spectrum, *MAPPINGS* assumes the metallicity and the shape of the EUV spectrum are defined (through the *STARBURST99* input), and characterizes the local ionization state by a local ionization parameter:

$$q = \frac{S_H \theta}{n} \quad (1)$$

where  $S$  is the ionizing photon flux through a unit area,  $n$  is the local number density of hydrogen atoms and  $q$  is the maximum velocity of an ionization front that can be driven by the local radiation field (Dopita 2000; Kewley & Dopita 2002). We used a 5 Myr continuous star-formation SED from *STARBURST99* as input to the *MAPPINGS III* code. The parameters of the SED consisted of a Saltpeter IMF with a power law of 2.35 and a star-formation rate of  $1 M_\odot \text{ yr}^{-1}$ .

We then constructed a series of plane parallel, isobaric models with  $P/k = 10^5 \text{ cm}^{-3} \text{ K}$ , where either the gas density, metallicity or the luminosity for the *STARBURST99* input were allowed to vary, with the other two variable remaining constant. For the *STARBURST99* input models, the density, metallicity and luminosity were varied as follows:

- **Density:**  $10\text{--}1000 \text{ cm}^{-3}$ ; metallicity ( $0.4Z_\odot$ ) and luminosity ( $10^{43}$  ergs) remain constant;
- **Metallicity:**  $0.05 - 2Z_\odot$ ; density ( $100 \text{ cm}^{-3}$ ) and luminosity ( $10^{43}$  ergs) remain constant;
- **Luminosity:**  $10^{41} - 10^{45}$  ergs; density ( $100 \text{ cm}^{-3}$ ) and metallicity ( $0.4Z_\odot$ ) remain constant.

Elemental abundances for  $0.5\text{--}2.0Z_\odot$  were adopted for the variable metallicity models, while for the variable density and luminosity models,  $0.4Z_\odot$  metallicity abundances were used.

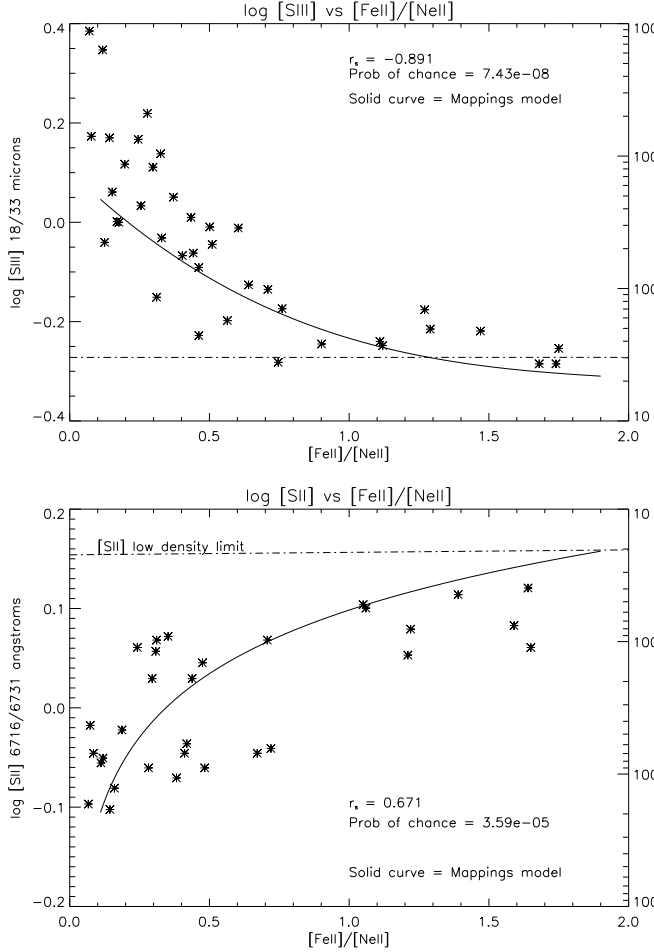


FIG. 5.— Plots of the [SIII] (top) and [SII] (bottom) ratios vs [FeII]/[NeII] for the extended galaxy sample, overlaid with model data from *MAPPINGS*. The dot-dash line indicates the low density limit.

Dust physics is treated explicitly through absorption, grain charging and photoelectric heating and the use of a standard MRN grain size distribution for both carbonaceous and siliceous grain types (Mathis, Rumpl & Nordsieck 1977). The *MAPPINGS* code took the undepleted solar abundances to be those of Anders & Grevesse (1989). For non-solar metallicities, *MAPPINGS* assumes that both the dust model and the depletion factors are unchanged. All elements except nitrogen and helium are taken to be primary nucleosynthesis elements. As for the shock models, we use the pre-run shock models from the *MAPPINGS* website, which are based upon a grid of  $n = 1.0$  models with  $v = 100$ - $1000$  km/s in steps of 25 km/s. The magnetic parameter  $B = p/\sqrt{n}$  is fixed to 3 in all calculations. This value corresponds to equipartition between thermal and magnetic pressures (Dopita & Sutherland 1996).

From the *MAPPINGS* output from the variable metallicity model, we saw that whilst the [SIII] and [SII] values remain relatively constant (and by extension, the density), the [FeII]/[NeII] ratio varies quite considerably. With the variable density model, interestingly, we saw that [FeII]/[NeII] does not drop with increasing density contrary to what we observe (Fig. 3), but rather

slightly increases, contrary to what we observe. Finally, for the variable luminosity model, both the [FeII]/[NeII] and unsurprisingly the [SIII] and [SII] values, remained constant. From the *MAPPINGS* model data, it would seem that the change in metallicity is primarily responsible for the observed drop in the [FeII]/[NeII] ratio. In order to directly compare the photoionization and shock model output with the IRS and optical data, we then set about defining models that would replicate the sort of density, metallicity and luminosity parameters typically seen in the sample. Since the low metallicity objects tend to have lower densities and luminosities, we generated *MAPPINGS* models that gradually increased the metallicity, density and luminosity, over the ranges outlined above, moving from low to high metallicity (0.05, 0.2, 0.4 and solar metallicity), low to high density ( $20$ - $1000$   $\text{cm}^{-3}$ ) and low to high luminosity ( $10^{42}$  to  $10^{44}$  ergs). As we increased the metallicity, we concurrently moved to high densities and higher luminosities. As with the earlier *MAPPINGS* models, we used a 5 Myr continuous star-formation SED from *STARBURST99* as input to the *MAPPINGS III* code (Leitherer et al. 1999). The parameters of the SED consisted of a Salpeter IMF with a power law of 2.35 and a star-formation rate of  $1 M_{\odot} \text{ yr}^{-1}$ . Elemental abundances for  $1/20 Z_{\odot}$ ,  $2/5 Z_{\odot}$  and  $1 Z_{\odot}$  were again adopted.

Using the observed [SII] 6716 & 6731 Å, [SIII] 18 & 33  $\mu\text{m}$  plus the [FeII] 26  $\mu\text{m}$  and [NeII] 12.8  $\mu\text{m}$  fluxes, we obtained the respective ratios and performed best fit line calculations to the [SIII] vs [FeII]/[NeII] and [SII] vs [FeII]/[NeII] model data, where the line fluxes are the product of both the photoionization and shock model outputs. Using the best fit models, we plotted the model ratio data in conjunction with the observed IRS and optical data ratios (Fig. 5), with the model data derived from the second *MAPPINGS* run describing very well the behaviour of both sets of observed line ratios.

#### 4.2.2. Cloudy models

The slight increase in the [FeII] emission with density seen from the *MAPPINGS* output poses the following question - where does this increase originate from? Is this increase due to an increased contribution to the [FeII] emission by dense HII regions and PDRs? If so, what is the level of this contribution? To resolve this, we used the spectral synthesis code Cloudy to try and determine how much of a contribution HII regions and PDRs make to the overall [FeII] emission, how this contribution is affected by the gas metallicity (as suggested by *MAPPINGS*), and the effect of the HII/PDR contribution has on the overall [FeII]/[NeII] ratio. We used the developmental version of the spectral synthesis code Cloudy, last described by Ferland et al. (1998). Abel et al. (2005) and Shaw et al. (2005) describe recent advances in its treatment of PDR chemistry, while van Hoof et al. (2004) describes the grain physics. As with the *MAPPINGS* models, we used a 5 Myr continuous star-formation SED from *STARBURST99* as input to Cloudy. The parameters of the SED consisted of a Salpeter IMF with a power law of 2.35 and a star-formation rate of  $1 M_{\odot} \text{ yr}^{-1}$ .

Our model geometry consists of a plane-parallel slab illuminated on one side by a source of UV radiation. Our calculations start at the hot, illuminated face of the slab,

where all the hydrogen is ionized. We end our calculations at two locations, when the hydrogen ionization fraction falls below 1% (for the pure H II region calculations, see below) and when the fraction of hydrogen in the form of  $H_2((2 \times n(H_2))/n(H)_{total})$  exceeds 90%. Beyond this depth, we expect there to be little contribution to either [FeII] or [NeII] emission.

We parameterize the ionizing continuum with the ‘ionization parameter’, which is the dimensionless ratio of hydrogen ionizing flux to density,

$$U = \frac{Q_H}{4\pi R^2 N_H c}$$

where  $Q_H$  is the total number of hydrogen-ionizing photons emitted by the central object per second. For all calculations, we chose  $\text{Log}[U] = -2.5$ , a value typical in H II regions (Veilleux & Osterbrock 1987). The ionization parameter in *MAPPINGS* is related to the one used in *Cloudy* by the equation:

$$U = \frac{q}{c} \quad (2)$$

We also include cosmic rays in our calculations. Primary and secondary cosmic ray ionization processes are treated as described in Appendix C of Abel et al. (2005), with an assumed cosmic ray ionization rate of  $5 \times 10^{-17} \text{ s}^{-1}$ . Cosmic rays are a significant heating source and also drive the ion-molecule chemistry deep in the molecular cloud. However, since our calculations stop short of the molecular cloud, for our models cosmic rays are only of secondary importance. Our calculations include the major ionization processes that can affect the ionization structure. This includes all stages of ionization for the lightest 30 elements.

Dust is known to play an important role in both H II regions and PDRs (Draine 2003). We self-consistently determine the grain temperature and charge as a function of grain size and material, for the local physical conditions and radiation field. This determines the grain photoelectric heating of the gas, an important gas heating process, as well as collisional energy exchange between the gas and dust. We also treat stochastic heating of grains as outlined in Guhathakurta & Draine (1989), which can affect the dust continuum shape. We include grain charge transfer as a general ionization - recombination process, as described in Appendix B of Abel et al. (2005). The rates at which  $H_2$  forms on grain surfaces is derived using the temperature and material-dependent rates given in Cazaux & Tielens (2002). The assumed grain size distribution is representative of the star-forming regions. The ratio of total to selective extinction,  $R_V = A_V/(A_B - A_V)$ , is a good indicator of the size distribution of grains (Cardelli et al. 1989). Calzetti et al. (2000) derived an average value for  $R_V \sim 4.3$ . We therefore use the  $R_V = 4$  grain size distribution given in Weingartner & Draine (2001). We also include size-resolved PAHs in our calculations, with the same size distribution used by Bakes & Tielens (1994). The abundance of carbon atoms in PAHs that we use,  $n_C(\text{PAH})/n_H$ , is  $3 \times 10^{-6}$ . PAHs are thought to be destroyed by hydrogen ionizing radiation and coagulate in molecular environments (see, for instance, Omont (1986)). We model this effect by scaling the PAH abundance by the ratio of  $H^0/H_{tot}(n_C(\text{PAH})/n_H = 3 \times 10^{-6} [n(H^0)/n(H_{tot})])$ .

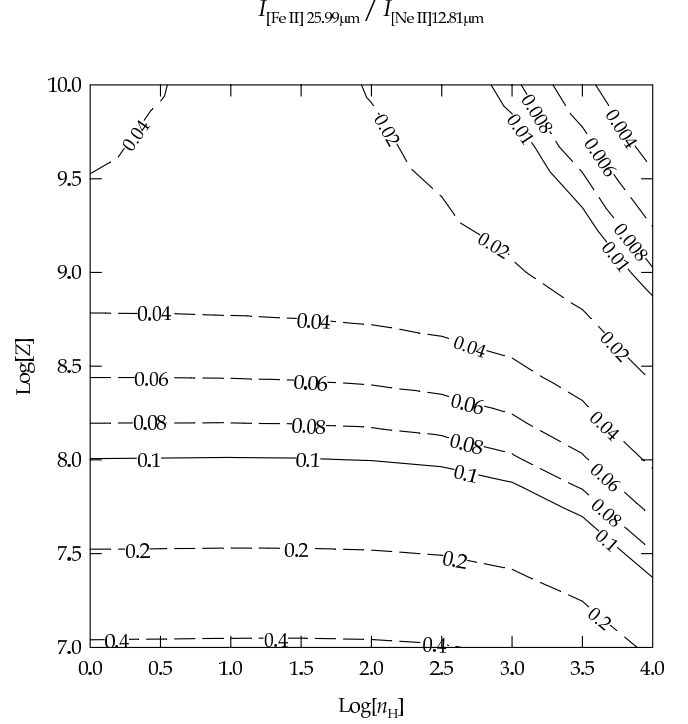


FIG. 6.— *Cloudy* photoionization model output of the [FeII]/[NeII] ratio as a function of density and  $Z$ , with contributions to the [FeII] emission by H II regions only.

The assumed gas-phase and dust abundances are extremely important in our calculations. We also assume gas-phase abundances based on an average of the abundances in the Orion Nebula derived by Baldwin et al. (1991), Rubin et al. (1991), and Osterbrock et al. (1992). The abundances by number are  $\text{He}/\text{H} = 0.095$ ,  $\text{C}/\text{H} = 3 \times 10^{-4}$ ,  $\text{O}/\text{H} = 4 \times 10^{-4}$ ,  $\text{N}/\text{H} = 7 \times 10^{-5}$ , and  $\text{Ar}/\text{H} = 3 \times 10^{-6}$ . We also assume default grain abundance of  $A_V/N(\text{H}_{tot}) = 5 \times 10^{-22} \text{ mag cm}^2$ . We then scale the metal and dust abundance such that the final value of  $Z = 12 + \text{Log}[\text{O}/\text{H}]$  ranges from 7 to 10, in increments of 1 dex.

There is one major exception to our assumed abundances, and that is the  $\text{Fe}/\text{H}$  ratio. Rodriguez & Rubin (2005) discuss the variation in  $\text{Fe}/\text{H}$  with  $Z$ , and as noted earlier, Izotov et al. (2006) also determined the variation in elemental abundances with  $Z$  from the Sloan Digital Sky Survey, including Ne and Fe. For these two elements, Izotov et al. (2006) provide the following equations to derive their respective abundances (for this work, we use the notation  $Z$  instead of  $X$ , as used in Izotov et al. (2006):

$$\text{Log}(\text{Ne}/\text{O}) = 0.097Z - 1.542 \quad (3)$$

and

$$\text{Log}(\text{Fe}/\text{O}) = -0.606Z + 2.994 \quad (4)$$

where  $Z = 12 + \text{Log}(\text{O}/\text{H})$ , we find that:

$$\text{Log} \left[ \frac{\text{Ne}}{\text{Fe}} \right] = -4.536 + 0.703Z. \quad (5)$$

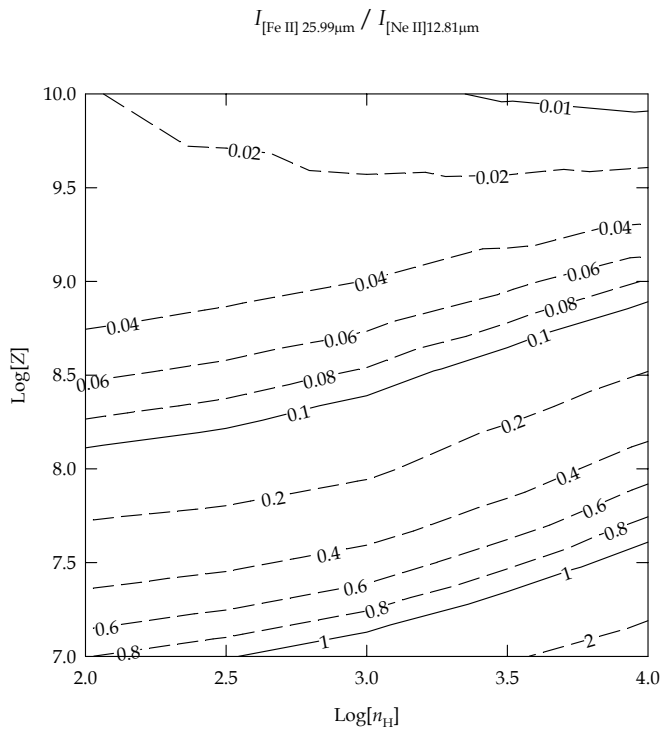


FIG. 7.— Cloudy photoionization model output of the  $[\text{FeII}]/[\text{NeII}]$  ratio as a function of density and  $Z$  with contributions to the  $[\text{FeII}]$  emission from both H II and PDR regions.

In all calculations, we scale the Fe abundance so that equation 3 is always obeyed.

The relationship between density, temperature, and pressure is determined by the assumed equation of state. We perform two sets of calculations, one where we stop the calculation at the hydrogen ionization front and one where we include the PDR. For the pure H II region models we assume constant density, with the density ranging from  $\text{Log}[n_H] = 0.5$  to  $\text{Log}[n_H] = 4$ , in increments of 0.5 dex. For the H II + PDR calculations, we assume constant pressure, with thermal and radiation pressure being the dominant contributors to the total pressure. We do not include turbulent pressure in the equation of state, although we assume a small turbulent broadening of  $1 \text{ km s}^{-1}$  for its effects on line optical depths. Such an equation of state neglects shocks or other time-dependent effects. In the constant pressure scenario, we specify  $n_H$  at the illuminated face, then solve for density based how the pressure contributions change with depth. Our densities range over  $\text{Log}[n_H] = 2$  to 4, in increments of 0.5 dex. Overall, our combination of  $n_H$  and  $Z$  represent 52 calculations.

In Fig. 6, we plot the  $[\text{FeII}]/[\text{NeII}]$  line ratio as a function of  $Z$  and density for the H II region only. In Fig. 7, we again plot the  $[\text{FeII}]/[\text{NeII}]$  line ratio as a function of  $Z$  and density, but this time including the PDR in addition to the H II region. As one can see, the relative H II contribution dominates over the PDR contribution at low densities (and metallicities), with the PDR contribution becoming more dominant as one moves to higher densities ( $\sim 10^3 \text{ cm}^{-3}$ ) and metallicities. Previous IR studies of starburst H II/PDR regions (Carral et al. 1994; Lord et al. 1996) support this scenario. For very dense

H II regions where the PDRs are irradiated by intense FUV, and thus PDR-derived  $[\text{FeII}]$  emission is dominant. Correspondingly at lower densities ( $\sim 10^2 \text{ cm}^{-3}$ ), the H II regions are larger, the PDRs lie further from the stars, and the resultant lowered FUV fluxes and densities do not excite  $[\text{FeII}]$  in the PDR, and thus the H II region dominates the H II/PDR contribution to  $[\text{FeII}]$  production for such environments.

#### 4.2.3. What is driving the Fe/Ne relationship?

From the *MAPPINGS* and *Cloudy* simulations and the comparisons with the IRS and optical data (Fig. 5), it would seem that metallicity is the primary driver for the behaviour of the  $[\text{FeII}]/[\text{NeII}]$  ratio, as metallicity determines the origin (shocks vs H II and/or PDRs) and strength of the  $[\text{FeII}]$  emission. We can reproduce the observed  $[\text{FeII}]/[\text{NeII}]$  dependence on  $Z$  if we assume the Izotov variation of  $\text{Fe}/\text{Ne}$  with  $Z$ . *Cloudy* reproduces the  $[\text{FeII}]/[\text{NeII}]$  ratio decrease with increases in density (for the pure H II region only) because of the following: the critical density for electron excitation of  $[\text{Fe II}]$  is  $1.2 \times 10^4 \text{ cm}^{-3}$ , while for  $[\text{Ne II}]$  it is  $5 \times 10^5 \text{ cm}^{-3}$ . The ratio of  $[\text{Fe II}]/[\text{NeII}]$  thus depends on the ratio:

$$\frac{(1 + n_{\text{critical}}(\text{neon})/n(H))}{(1 + n_{\text{critical}}(\text{iron})/n(H))}$$

In the low density limit, this ratio is  $\sim 42$ . However, for a density of  $1 \times 10^4 \text{ cm}^{-3}$ , which is the high end of our parameter space, this ratio is only  $\sim 20$  because  $[\text{Fe II}]$  emission is suppressed by the higher density. The reason the ratio increases with density in Fig. 7 (H II + PDR) is because  $[\text{Fe II}]$  is excited by atomic hydrogen in the PDR in addition to electrons in the H II region. The critical density of  $[\text{Fe II}]$  with H atoms is  $\sim 1 \times 10^6 \text{ cm}^{-3}$ . Therefore  $[\text{Fe II}]$  emits readily in the PDR, while  $[\text{Ne II}]$  does not emit because all the neon is neutral. However, we do note that the H II and PDR contribution to the  $[\text{FeII}]$  emission is surpassed by the contribution from shocks at the lowest metallicities and densities, based on comparison with the *MAPPINGS* output and the observed data - perhaps only  $\sim 10\%$  of the  $[\text{FeII}]$  emission comes from H II and PDRs with that contribution rising to  $\sim 80\text{--}90\%$  as one moves to higher metallicity. As we move to roughly solar metallicity, it would seem likely that the dominant mechanism for production of  $[\text{FeII}]$  (and thus the behaviour of the  $[\text{FeII}]/[\text{NeII}]$  ratio at high metallicities) is from H II and PDRs in combination rather than from SNe shocks.

#### 4.2.4. Can we tie in the behaviour of the gas density with the $[\text{FeII}]/[\text{NeII}]$ ratio, metallicity and PAH strength?

While abundances may play a role in the overall behavior of the  $[\text{FeII}]/[\text{NeII}]$  ratio, the shock scenario would seem to fit the observed variation of the gas density and the PAH ratio with metallicity. Assuming that shocks are indeed behind the observed correlations, the following scenarios would seem to account for the relationship between the  $[\text{FeII}]/[\text{NeII}]$  and  $[\text{SiII}]$  ratios and the PAH strength. In very low metallicity dwarf starburst environments, such as I Zw 18, the observed gas density is phenomenally low, in the order of  $\sim 20\text{--}100 \text{ cm}^{-3}$ . From Fig. 3 and the models, it would seem that low density correlates strongly with the presence of strong supernovae

shocks, a harsh radiation environment which is lacking in populations of dust and PAH, as noted by the lack of PAH emission (Figs. 1 and 4) and generally flat slopes of the dust continua. It would seem likely therefore that we are probing the tenuous gas within a superbubble cavity that has been carved by the cumulative effects of numerous supernova-driven shocks. Previous surveys of low metallicity dwarf galaxies have found evidence for such superbubbles (Strickland & Stevens 2000; Calzetti et al. 2004; Ott et al. 2005), with ionized gas expanding at a rate of several tens of km/s driven by mechanical energy from starbursts deposited into the ISM (Calzetti et al. 2004).

For high metallicity environments, the picture becomes somewhat more complicated. Such objects are of course still the sites of high levels of massive star formation - the high metallicity starburst M82 is after all the template for starburst activity - but we see a much more benign environment for the survivability of dust and PAH. A number of new factors play a role in affecting star formation and its effects on the local environment. First of all, from the *Cloudy* and *MAPPINGS* models plus the observed data, we note that the dominant contribution to the [FeII] flux no longer comes from shocks, but rather from HII regions and from PDRs in particular - the lack of shocks propagating into the ISM provides a more benign, denser environment for the build-up of dust and PAH. Superbubbles are present as in low metallicity galaxies, however supernova-driven shocks are no longer the dominant mechanism driving the expansion but rather stellar winds from massive stars. As a consequence, less mechanical energy is available to drive breakout and outflow and the superbubble can remain enclosed, especially where the gravitational potential of the galaxy is steep (Skillman & Bender 1995; Burkert 2004; Calzetti et al. 2004). Given the inability of weaker shocks to drive out material and clear the local ISM, it is not surprising that we should see a buildup of metals, and the survivability of dust and PAH formed locally.

#### 4.2.5. Are abundances driving the $Fe/Ne$ relationship?

Whilst the SNe-driven shock hypothesis is convincing in terms of the enhanced [FeII] emission and corresponding low PAH emission, it is not the only plausible explanation for the observed correlation. As we have already noted, from Izotov et al. (2006) it has been suggested that the observed levels of [FeII] emission may instead be abundance driven. Using equations 1 & 2 to derive how the  $Fe/Ne$  ratio varies with metallicity, we see that the  $Fe/Ne$  ratio decreases with increasing  $Z$  in a fashion very similar to the [FeII]/[NeII] vs.  $Z$  correlation, suggesting that the variation in the [FeII]/[NeII] emission ratio with  $Z$  may be a consequence of varying  $Fe/Ne$  abundance with  $Z$ . Indeed, the slope of  $Fe/Ne$  vs.  $Z$  from Izotov et al. (2006) is very similar to the slope of the best fitting line from Fig 2 ( $m = -0.68$ ) - our observational dataset points to this being a possibility, and the *MAPPINGS* and *Cloudy* models further lend support to this scenario.

However given the similarity in terms of behaviour of our observational dataset with the Izotov et al. (2006) results, it begs the question - what may be causing the change in  $Fe/Ne$  with  $Z$ ? Since neon is not depleted (Juett et al. 2006; Yao et al. 2006), the observed rela-

tionship would then be due to variations in  $Fe/H$  rather than  $Ne/H$ . So what is causing the iron depletion? Since iron is known to be depleted onto grains (Juett et al. 2006; Yao et al. 2006), the increased variation in  $Fe/H$  would suggest that there is either more grain destruction, or less grain formation, as one moves to lower metallicities.

If this is correct, the reason for the observed [FeII]/[NeII] with  $Z$  trend is that Fe is less depleted in low metallicity galaxies. This would have a profound impact on ISM studies, as the usefulness of iron emission as a pure indicator of shocks may be compromised. However, this is not conclusive, and we need more observations to deduce for certain the physical process which is controlling the [FeII] emission. In order to definitively figure out if shocks are truly responsible for the [FeII] emission at low metallicity, we require high resolution IR spectroscopy to unambiguously determine the presence of shocks within the velocity profiles. The upcoming availability of such high resolution spectroscopic data from *Herschel* and *SOFIA* will be crucial to determine the true nature of iron emission at low metallicity and we look forward to furthering this line of investigation in a future paper.

## 5. CONCLUSIONS

Using archival *Spitzer* observations of 41 starburst galaxies that span a wide range in metallicity, we found a correlation between the ratio of emission line fluxes of [FeII] at  $26\ \mu\text{m}$  and [NeII] at  $12.8\ \mu\text{m}$  and the electron gas density as traced by the  $18.7/33.4\ \mu\text{m}$  [SIII] ratio, with the [FeII]/[NeII] flux ratio decreasing with increasing gas density. We also find a strong correlation between the gas density and the PAH peak to continuum strength. The correlation of the [FeII]/[NeII] ratio and the PAH peak to continuum strength found in O'Halloran, Satyapal & Dudik (2006) was confirmed for a larger sample. Using shock and photoionization models, we see that metallicity is the primary driver for the observed behaviour of the [FeII]/[NeII] ratio. It may very well be that the majority of [FeII] emission at low metallicity may be shock-derived, whilst at high metallicity, the [FeII] emission is dominated by contributions from HII and in particular, from PDR regions, and that at higher metallicity shocks may not play as significant a role in removing gas, PAH and dust from the ISM, unlike in low metallicity systems. However, the observed [FeII]/[NeII] emission may instead be following a metallicity-abundance relationship, with the iron being less depleted in low metallicity galaxies, a result that would have profound implications for the use of Fe emission lines as unambiguous tracers of shocks. Follow up high resolution spectroscopic observations will be required to determine if this is indeed the case, or if the detected iron emission is truly tracing emission from the passage of shocks.

We are grateful to S. Satyapal for her comments and guidance. BO'H gratefully acknowledges financial support from NASA grant NAG5-11432. NPA acknowledges National Science Foundation support under Grant No. 0094050, 0607497 to The University of Cincinnati. This work is based on archival data obtained with the *Spitzer* Space Telescope, which is operated by the Jet Propulsion



Laboratory, California Institute of Technology under a contract with NASA. The IRS was a collaborative venture between Cornell University and Ball Aerospace Corporation funded by NASA through the Jet Propulsion Laboratory and Ames Research Center. *SMART* was de-

veloped at Cornell University and is available through the *Spitzer* Science Center at Caltech. The *SPICE* reduction package has been developed by and released through the *Spitzer* Science Center.

## REFERENCES

- Abel N.P., Ferland G.J., Shaw G. & van Hoof P.A.M., 2005, ApJS, 161, 65
- Anders E. & Grevesse N., 1989, *Geochimica et Cosmochimica Acta*, 53, 197
- Bakes E.L.O. & Tielens A.G.G.M., 1994, ApJ, 427, 822
- Baldwin J.A., Ferland G.J., Martin P.G. et al., 1991 ApJ, 374, 580
- Brandl B.R., Devost D., Higdon S.J.U. et al., 2004, ApJS, 154, 188
- Burkert A., 2004, *The Formation and Evolution of Massive Young Star Clusters*, ASP Conference Series, vol. 322., p.489
- Calzetti D., Armus L., Bohlin R.C. et al., 2000, ApJ, 533, 682
- Calzetti D., Harris J., Gallagher J. et al., 2004, AJ, 127, 1405
- Cardelli J.A., Clayton G.C. & Mathis J.S., 1989, ApJ, 345, 245
- Carral P., Hollenbach D.J., Lord S.D. et al., 1994, ApJ, 423, 223
- Cazaux S. & Tielens A.G.G.M., 2002, ApJ, 575, 29
- Dopita M.A. & Sutherland R.S., 1996, ApJS, 102, 61
- Dopita M.A., 2000, Ap&SS, 272, 79
- Draine B. T., 1989, *Interstellar Extinction in the Infrared*, European Space Agency, p.93.
- Draine B.T., 2003, ARA&A, 41, 241
- Dudik R.P., Weingartner J.C., Satyapal S. et al., 2007, ApJ, 684, 71.
- Ferland G.J., Korista K.T., Verner D.A. et al., 1998, PASP, 110, 761
- Förster Schreiber, N. M., Roussel, H., Sauvage, M., Charmandaris, V., 2004, A&A, 419, 501
- Galliano F., Dwek E. & Charnial P., 2008, ApJ, 672, 214
- Guhathakurta P. & Draine B.T., 1989, ApJ, 345, 230
- Higdon S.J.U., Devost D., Higdon J.L. et al., 2004, PASP, 116, 975
- Hogg D.W., Tremonti C.A., Blanton M.R. et al., 2005, A&A, 388, 439
- Hoyos C. & Diaz A.I., 2006, MNRAS, 365, 454
- Ho L.C., Filippenko A.V. & Sargent W.L.W., 1997 ApJS, 112, 315
- Izotov Y.I. & Thuan T.X., 2002, ApJ, 567, 875
- Izotov Y.I., Papaderos P., Guseva N.G. et al., 2004, A&A, 421, 539
- Izotov Y.I., Stasinska G., Meynet G. et al., 2006, A&A, 448, 955
- Juett A.M., Schulz N.S., Chakrabarty D., Gorczyca T.W., 2006, ApJ, 648, 1066
- Kendall M. & Stuart A. 1976, In: *The Advanced Theory of Statistics*, Vol. 2, Macmillian
- Kewley L.J., Dopita M.A., Sutherland R.S., Heisler C.A. & Trevena J., 2001, ApJ, 556, 121
- Kewley L.J. & Dopita M.A., 2002, ApJS, 142, 35
- Kong X. & Cheng F.Z., 1999, A&A, 351, 477
- Leitherer C., Schaerer D., Goldader J.D. et al., 1999, ApJS, 123, 3
- Lord S.D., Hollenbach D.J., Haas M.R. et al., 1996, ApJ, 465, 703
- Lutz D., Veilleux S., & Genzel R., 1999, ApJ517, 13
- Madden S.C., Galliano F., Jones A.P. & Sauvage, M., 2006, A&A, 446, 877
- Mathis J.S., Ruml W. & Nordsieck, K. H., 1977, ApJ, 217, 425
- O'Halloran B., Satyapal S. & Dudik R.P., 2006, ApJ, 641, 795
- Omout A., 1986, A&A, 164, 159
- Osterbrock D.E., Tran H.D. & Veilleux S., 1992, ApJ, 389, 305
- Ott J., Walter F. & Brinks E., 2005, MNRAS, 358, 1423
- Reach W.T. & Rho J., 2000, ApJ, 544, 843
- Reach W.T., Rho J., Tappe A. et al., 2006, AJ, 131, 479
- Rigopoulou D., Lutz D., Genzel R. et al., 1996, A&A, 315, 125
- Rigopoulou, D., Spoon, H. W. W., Genzel, R. et al., 1999, AJ, 118, 2625
- Rodriguez M. & Rubin R.H., 2005, ApJ, 626, 900
- Rubin R.H., Simpson J.P., Haas M.R. & Erickson E.F., 1991, ApJ, 374, 564
- Satyapal S., Dudik R.P., O'Halloran B. & Gliozzi M., 2005, ApJ, 633, 86
- Scoville N.Z., Evans A.S., Thompson R. et al., 2000, AJ, 119, 991
- Shaw G., Ferland G.J., Abel N.P. et al., 2005, ApJ, 624, 794
- Skillman E.D. & Bender R., 1995, RMxAC, 3, 255
- Smith B.J., Struck C. & Nowak M.A., 2005, AJ, 129, 1350
- Storey, P.J. & Hummer D.G., 1995, MNRAS, 272, 41
- Strickland D.K. & Stevens I.R., 2000, MNRAS, 304, 511
- Sturm E., Lutz D., Tran D. et al., 2000, A&A358, 481
- Surace J.A. & Sanders D. B., 1999, ApJ, 512, 162
- Sutherland R.S. & Dopita M.A., 1993, ApJS, 88, 253
- Thomas H.C., Dunne L., Clemens, M.C. et al., 2002, MNRAS, 329, 747
- Vacca W. & Conti P., 1992, ApJ, 401, 543
- van Hoof P.A.M., Weingartner J.C., Martin P.G. et al., 2004, MNRAS, 350, 1330
- Verma A., Lutz D., Sturm E. et al., 2004, A&A, 403, 829
- Veilleux S. & Osterbrock D.E., 1987, ApJS, 63, 295
- Weingartner J.C. & Draine B.T., 2001, ApJ, 548, 296
- Wu Y., Charmandaris V., Hao L. et al., 2006, ApJ, 639, 157
- Yao Y., Schulz N., Wang Q.D. & Nowak M., 2006, ApJ, 653, 121

TABLE 1. IRS FLUX DATA.

Target	Metallicity 12+log(O/H)	F([NeII]) @ 12.8 $\mu\text{m}$ ( $\times 10^{-20} \text{ W cm}^{-2}$ )	F([SIII]) @ 18.7 $\mu\text{m}$ ( $\times 10^{-20} \text{ W cm}^{-2}$ )	F([FeII]) @ 26.0 $\mu\text{m}$ ( $\times 10^{-20} \text{ W cm}^{-2}$ )	F([SIII]) @ 33.4 $\mu\text{m}$ ( $\times 10^{-20} \text{ W cm}^{-2}$ )
(1)	(2)	(3)	(4)	(5)	(6)
I Zw 18	7.2	0.030 $\pm$ 0.003	0.006 $\pm$ 0.001	0.051 $\pm$ 0.015	0.011 $\pm$ 0.006
SBS 0335-052	7.3	0.014 $\pm$ 0.003	0.013 $\pm$ 0.003	0.018 $\pm$ 0.006	0.021 $\pm$ 0.008
HS 2236+1344	7.5	0.032 $\pm$ 0.002	0.063 $\pm$ 0.008	0.056 $\pm$ 0.016	0.112 $\pm$ 0.011
SDSS J0519+0007	7.5	0.207 $\pm$ 0.014	0.048 $\pm$ 0.014	0.155 $\pm$ 0.056	
SBS 1415+437	7.6	0.068 $\pm$ 0.013	0.026 $\pm$ 0.007	0.076 $\pm$ 0.024	0.045 $\pm$ 0.021
HS 0837+4717	7.6	0.121 $\pm$ 0.010	0.020 $\pm$ 0.005	0.177 $\pm$ 0.036	0.033 $\pm$ 0.011
Tol 65	7.6	0.024 $\pm$ 0.013	0.011 $\pm$ 0.002	0.040 $\pm$ 0.005	0.022 $\pm$ 0.008
HS 1442+4250	7.6	0.226 $\pm$ 0.010	0.024 $\pm$ 0.004	0.127 $\pm$ 0.041	0.038 $\pm$ 0.004
Mrk 25	7.8	1.074 $\pm$ 0.156	0.847 $\pm$ 0.104	0.647 $\pm$ 0.128	0.870 $\pm$ 0.026
SBS 1030+583	7.8	0.075 $\pm$ 0.014	0.167 $\pm$ 0.011	0.028 $\pm$ 0.007	0.149 $\pm$ 0.043
Mrk 209	7.8	0.068 $\pm$ 0.017	0.070 $\pm$ 0.024	0.077 $\pm$ 0.020	0.124 $\pm$ 0.024
Mrk 36	7.9	0.281 $\pm$ 0.071	0.051 $\pm$ 0.010	0.130 $\pm$ 0.024	0.085 $\pm$ 0.006
SBS 0917+527	7.9	0.228 $\pm$ 0.058	0.115 $\pm$ 0.024	0.074 $\pm$ 0.007	0.084 $\pm$ 0.008
SBS 1152+579	7.9	0.928 $\pm$ 0.300	0.071 $\pm$ 0.037	0.305 $\pm$ 0.018	0.076 $\pm$ 0.024
Mrk 170	7.9	0.053 $\pm$ 0.015	0.033 $\pm$ 0.002	0.048 $\pm$ 0.006	0.058 $\pm$ 0.009
UM 448	8.0	1.430 $\pm$ 0.018	0.397 $\pm$ 0.031	0.442 $\pm$ 0.084	0.563 $\pm$ 0.099
SBS 0946+558	8.0	0.053 $\pm$ 0.015	0.034 $\pm$ 0.022	0.026 $\pm$ 0.003	0.034 $\pm$ 0.006
II Zw 40	8.1	0.452 $\pm$ 0.061	1.375 $\pm$ 0.026	0.115 $\pm$ 0.031	1.274 $\pm$ 0.304
Mrk 930	8.1	0.219 $\pm$ 0.074	0.170 $\pm$ 0.019	0.112 $\pm$ 0.026	0.189 $\pm$ 0.056
Mrk 996	8.1	0.297 $\pm$ 0.022	0.271 $\pm$ 0.044	0.073 $\pm$ 0.011	0.184 $\pm$ 0.046
Tol 1924-416	8.1	0.464 $\pm$ 0.039	0.247 $\pm$ 0.050	0.058 $\pm$ 0.001	0.271 $\pm$ 0.073
II Zw 70	8.1	0.143 $\pm$ 0.012	0.178 $\pm$ 0.041	0.182 $\pm$ 0.053	0.268 $\pm$ 0.075
NGC 4670	8.2	0.482 $\pm$ 0.173	0.240 $\pm$ 0.039	0.309 $\pm$ 0.042	0.321 $\pm$ 0.029
Mrk 450	8.2	0.125 $\pm$ 0.009	0.083 $\pm$ 0.029	0.050 $\pm$ 0.015	0.096 $\pm$ 0.059
Mrk 5	8.2	0.106 $\pm$ 0.013	0.076 $\pm$ 0.020	0.075 $\pm$ 0.019	0.103 $\pm$ 0.027
Mrk 1329	8.2	0.305 $\pm$ 0.015	0.257 $\pm$ 0.054	0.060 $\pm$ 0.002	0.196 $\pm$ 0.036
NGC 5253	8.2	0.572 $\pm$ 0.075	1.172 $\pm$ 0.039	0.434 $\pm$ 0.100	1.749 $\pm$ 0.249
IC 342	8.3	34.239 $\pm$ 5.285	9.902 $\pm$ 0.156	5.793 $\pm$ 0.025	9.872 $\pm$ 1.771
Haro 3	8.3	2.016 $\pm$ 0.084	1.431 $\pm$ 0.064	0.306 $\pm$ 0.042	1.243 $\pm$ 0.090
UM 311	8.3	0.126 $\pm$ 0.010	0.0873 $\pm$ 0.021	0.056 $\pm$ 0.009	0.101 $\pm$ 0.042
Mrk 1499	8.4	0.150 $\pm$ 0.014	0.319 $\pm$ 0.008	0.069 $\pm$ 0.017	0.393 $\pm$ 0.018
UGC 4274	8.5	0.710 $\pm$ 0.030	0.402 $\pm$ 0.036	0.308 $\pm$ 0.079	0.393 $\pm$ 0.093
NGC 7793	8.7	0.318 $\pm$ 0.077	0.295 $\pm$ 0.010	0.088 $\pm$ 0.025	0.178 $\pm$ 0.069
NGC 4194	8.8	8.464 $\pm$ 0.169	2.151 $\pm$ 0.042	1.491 $\pm$ 0.336	2.151 $\pm$ 0.466
NGC 253	8.9	199.753 $\pm$ 1.235	42.928 $\pm$ 0.780	28.433 $\pm$ 1.154	29.012 $\pm$ 0.416
He 2-10	8.9	24.671 $\pm$ 1.677	9.034 $\pm$ 0.156	2.300 $\pm$ 0.091	6.072 $\pm$ 0.990
NGC 7714	8.9	8.546 $\pm$ 0.169	2.665 $\pm$ 0.016	1.012 $\pm$ 0.121	1.200 $\pm$ 0.194
M82	9.0	948.875 $\pm$ 25.765	44.638 $\pm$ 0.047	66.546 $\pm$ 2.118	18.416 $\pm$ 0.411
NGC 3049	9.0	2.800 $\pm$ 0.353	1.008 $\pm$ 0.180	0.834 $\pm$ 0.016	0.780 $\pm$ 0.104
NGC 1482	9.1	100.483 $\pm$ 4.179	13.346 $\pm$ 0.104	1.759 $\pm$ 0.073	4.905 $\pm$ 0.119
NGC 2903	9.3	84.257 $\pm$ 1.871	4.456 $\pm$ 0.026	7.563 $\pm$ 0.057	1.979 $\pm$ 0.267

NOTE. — Columns: (1) Common source names; (2) Metallicity of the galaxy; (3) Extinction corrected flux of the 12.8  $\mu\text{m}$  [NeII] fine structure line in Watts per centimeter squared; (4) Extinction corrected flux of the 18.7  $\mu\text{m}$  [SIII] fine structure line in Watts per centimeter squared; (5) Extinction corrected flux of the 26.0  $\mu\text{m}$  [FeII] fine structure line in Watts per centimeter squared; (6) Extinction corrected flux of the 33.4  $\mu\text{m}$  [SIII] fine structure line in Watts per centimeter squared.

TABLE 2. IRS AND OPTICAL FLUX RATIOS.

Target (1)	PAH 6.2 micron P/C (2)	[FeII]/[NeII] (3)	log ([SIII] 18.7/33.4 $\mu$ m) (4)	log ([SII] 6716/6731 Å) (5)
I Zw 18	1.2	1.74	-0.29	1.32 <sup>a</sup>
SBS 0335-052	1.23	1.29	-0.22	1.2 <sup>b</sup>
HS 2236+1344	1.88	1.75	-0.25	1.15 <sup>c</sup>
SDSS J0519+0007	1.89	0.75	1.17 <sup>c</sup>	
SBS 1415+437	1.57	1.11	-0.24	1.15 <sup>b</sup>
HS 0837+4717	1.66	1.47	-0.22	1.1 <sup>c</sup>
Tol 65	1.41	1.68	-0.29	1.21 <sup>c</sup>
HS 1442+4250	1.81	0.56	-0.20	-
Mrk 25	2.56	0.60	-0.11	-
SBS 1030+583	1.67	0.37	0.05	1.25 <sup>b</sup>
Mrk 209	2.27	1.12	-0.25	1.28 <sup>a</sup>
Mrk 36	1.82	0.46	-0.23	1.07 <sup>b</sup>
SBS 0917+527	2.1	0.33	0.04	1.14 <sup>b</sup>
SBS 1152+579	2.41	0.33	-0.14	1.17 <sup>b</sup>
Mrk 170	2.2	0.90	-0.25	
UM 448	1.63	0.31	-0.15	1.07 <sup>b</sup>
SBS 0946+558	2.5	0.50	-0.01	1.11 <sup>b</sup>
II Zw 40	2.6	0.26	0.03	1.15 <sup>b</sup>
Mrk 930	2.5	0.51	-0.04	1.15 <sup>b</sup>
Mrk 996	3.3	0.24	0.17	-
Tol 1924-416	2.8	0.13	-0.04	1.13 <sup>b</sup>
II Zw 70	2.1	1.27	-0.18	1.2 <sup>b</sup>
NGC 4670	3.75	0.64	-0.13	-
Mrk 450	2.64	0.40	-0.07	1.17 <sup>c</sup>
Mrk 5	2.91	0.71	-0.13	1.11 <sup>b</sup>
Mrk 1329	3.88	0.40	0.07	1.06 <sup>c</sup>
NGC 5253	3.21	0.71	-0.13	0.91 <sup>b</sup>
IC 342	3.42	0.17	0.00	0.83 <sup>e</sup>
Haro 3	4.18	0.15	0.06	1.23 <sup>a</sup>
UM 311	3.27	0.44	-0.06	0.92 <sup>b</sup>
Mrk 1499	4.27	0.46	-0.09	-
UGC 4274	3.92	0.43	0.01	0.9 <sup>e</sup>
NGC 7793	4.78	0.28	0.22	-
NGC 4194	3.66	0.18	0.00	-
NGC 253	3.05	0.14	0.17	-
He 2-10	4.1	0.08	0.17	1.04 <sup>f</sup>
NGC 7714	4.22	0.12	0.35	0.88 <sup>b</sup>
M82	5.07	0.07	0.38	0.8 <sup>e</sup>
NGC 3049	5.23	0.30	0.11	0.87 <sup>b</sup>
NGC 1482	3.7	0.02	0.43	-
NGC 2903	5.26	0.09	0.35	1.11 <sup>e</sup>

NOTE. — Columns:(1) Common source names; (2) PAH 6.2 micron peak to continuum ratio; (3) [FeII]/[NeII] line ratio; (4) Logarithm of the [SIII] 18.7 to 33.4 micron line ratio; (5) Logarithm of the [SII] 6716 to 6731 Å line ratio. Sources for [SII] ratios (a): Kong & Cheng (1999); (b) Hoyos & Diaz (2006); (c) Izotov et al. (2004); (d) Izotov & Thuan (2002); (e) Ho et al. (1997); (e) Ho et al. (1997); (e) Vacca & Conti (1992).